



# Octagonal flower-shaped wideband polarization insensitive metamaterial absorber for solar harvesting application

Md Raihan<sup>1</sup> · Sikder Sunbeam Islam<sup>1</sup> · Abidur Rahman Shuvo<sup>1</sup>

Received: 2 September 2023 / Accepted: 8 April 2024 / Published online: 29 April 2024  
© The Author(s), under exclusive licence to Springer-Verlag GmbH Germany, part of Springer Nature 2024

## Abstract

Metamaterial absorbers (MMA) attract great interest due to their unique properties. For energy harvesting from solar MMA in the optical region having wide bandwidth is one of the top research sectors nowadays. Our main solar source is the sun which includes UV, NIR and visible wavelength. Among them, the visible wavelength is most important for harnessing energy. Absorber operating in this region has a variety of application fields. In this study, the process of achieving a high absorption rate for total solar visible wavelength is being proposed. Various properties of the proposed MMA have also been analyzed to comprehend its characteristics. Geometric analysis was performed to optimize the design and output characteristics for optimal value and probable application. Cross and co-polarization, along with PCR (Polarization Conversion Ratio) verification, were also evaluated. The proposed MMA operates for full visible wavelength spanning 380 nm to 700 nm. It has an absorption rate of 97.8% and peak absorption of 99.9%. An above 90.8% absorption level was achieved throughout the operating wavelength. Furthermore, this absorber is totally polarization insensitive and the incident angle is independent up to 70°. A comprehensive parametric assessment has been conducted to accurately characterize the absorber and understand how the results are derived. Finite Integration Technique (FIT) has been employed for calculating absorbance and reflectance. The proposed model shows similar absorbance across TEM, TE, and TM waveguide propagation modes. Furthermore, the constancy of the polarization angle has been validated. Because of the excellent metamaterial properties, the proposed metamaterial absorber can be used for optical range, solar harvesting, solar cell, and solar thermophotovoltaic (STPV) applications. It can be used for light-detecting and sensing applications as well.

**Keywords** Metamaterial absorber · Wideband · Polarization Insensitive · Flower shaped · Solar harvesting

## 1 Introduction

For ages, scientists have tried to control the properties of light and sound as they interact with our sensory systems. They have tried to get control over electromagnetic waves to manipulate them according to their will. Victor Veselago, the Russian physicist, invented left-handed materials [1] in 1967, setting the base for metamaterials. A metamaterial [2] is a new artificially engineered material for manipulating electromagnetic waves. They possess some extraordinary characteristics, such as negative permittivity [3–5], negative permeability [6] and negative refractive

index [7], that natural material cannot. These distinct properties enable nanoscale light manipulation [8], leading to the development of ground-breaking technologies such as super lenses [9, 10], invisibility cloaks [11, 12], and perfect absorbers [13–15]. Furthermore, metamaterials can manipulate waves at a wide variety of frequencies, including radio waves, microwaves [16–18], terahertz waves [19, 20], and even optical frequencies [21–23]. Since the concept was developed by Victor Veselago, researchers have tried to break the limitation of prior work. Advancement in this field leads them to unlock various exclusive features. Metamaterial absorbers absorb specific frequencies, which makes it suitable for various applications such as sensing [24–26], imaging [27, 28], detecting [29, 30], energy harvesting [31, 32] and so on. MMA now used in satellite communication [33–35], antenna system [36–43], and in biomedical sector [44, 45], telecommunication [46–48], radar applications [49, 50]. The range of applications in

✉ Md Raihan  
mohammedraihan133@gmail.com

<sup>1</sup> Department of Electrical and Electronic Engineering,  
International Islamic University Chittagong,  
Chittagong 4318, Bangladesh

this area grows daily, and the door of many application fields is opened by metamaterial. Metamaterials are also used in acoustics and vibration control to reduce noise [51–53] and soundproofing [54, 55]. They also have sub-applications such as superlensing [56–58], and electromagnetic shielding [59, 60], breast imaging [61–63], head imaging [64]. Potential future fields for metamaterials as research improves include quantum technology [65, 66], wearable electronics [67, 68], robotics [69, 70], deep learning based metamaterial for antenna, IOT [71, 72], and environmental sensing [73]. Collecting energy from solar using metamaterial draws significant attention due to the easy fabrication process and absorption efficiency. Researchers are trying to break the barrier of some limitations that are still faced in MMA. This [74] research shows a structures and manufacturing of an MMA made of TiN material with efficient and wide-spectrum light absorption. Across the range of 400–800 nm, the absorber with a thickness of 240 nm exhibits absorption characteristics that remain unaffected by polarization, exceeding 87% and often reaching over 95% absorption, especially around 650 nm where it achieves near-complete absorption with an average of approximately 95% within this spectral range. This [21] research proposes a visible spectrum metamaterial absorber using tungsten-based fractal architecture, achieving over 90% absorbance within 400–750 nm. It maintains steady absorption (above 70%) over incident angles of 0°–60° under the TE mode. Tungsten-based fractal architecture achieves 90% absorbance within 400–750 nm, maintaining steady absorption under transverse electric mode [75]. The study [76] presents a DSR metamaterial absorber (MMA) capable of absorbing all visible optical wavelengths with TE and TM modes that is independent of polarization. It attains an average absorption rate of 97% over the entire visible range, with constant absorption qualities demonstrated through the application of the interference theory (IT) model and the assessment of the polarization conversion ratio (PCR). A study [77] proposed a highly effective transparent metamaterial absorber (MMA) with near-perfect absorbance (> 90%) over a wide frequency range 301 THz to 844 THz, relative bandwidth of 94.8%). The MMA demonstrated polarization insensitivity and stable absorbance (> 80%) at broad angles within specific geometric parameters.

In this paper we proposed a metamaterial absorber with high absorption that is about 97.8% in average throughout the whole wavelength. This compact MMA is designed using the material Tungsten and silicon dioxide to meet the optical absorption properties. It shows wide incident angle up to 70° and shows excellent Polarization insensitivity. we've analyzed the MMA with different material to see the output and potential application. The MMA can

be used as solar harvesting, light detector, sensing, Solar thermophotovoltaics etc.

## 2 Material choices

Perfect material choice is an important factor to achieve desired output from a design. For absorber working perfectly without losing its thermal and optical property, temperature stability is a crucial part. Several studies have shown that absorbers made of refractory metals are effective at absorbing electromagnetic radiation. Their availability, high costs, and low melting points, however, limit their efficiency in certain applications, such as solar thermophotovoltaics [78–80]. Moreover, considering our intended operating wavelength within the optical region, it is crucial for the chosen material to endure high-frequency temperatures. Due to its favorable impedance match in free space and minimal ohmic losses we have selected Tungsten (W) as both our metal resonator and blocking plate material. The high melting point of this metal, at 3422 °C [81] renders it suitable for use in high-temperature environments. Furthermore, its electrical conductivity of  $1.89 \times 10^7$  (S/m) enhances its suitability for such conditions. The primary benefit of utilizing tungsten lies in its ability to amplify light absorption within the spectrum's shorter wavelengths [82]. Due to its favorable impedance match in free space and minimal ohmic losses, Tungsten emerges as a suitable candidate for both resonator and ground layer applications. The precise configuration of the physical structure plays an important role in detecting the resonance wavelength. These resonance characteristics primarily arise from the dissipation of electromagnetic wave energy within the absorber's electromagnetic resonance mode and the field dissipation effect induced by the substantial imaginary component of the tungsten metal layer. When compared to alternative refractory metals, tungsten (W) possesses a diminished vapor pressure and a low infrared emissivity [83]. It is a potential material for optical regime metamaterial absorbers because it absorbs a significant amount of electromagnetic energy in the visible and near-infrared regions [84]. In nanotechnology, silicon dioxide (SiO<sub>2</sub>) is a highly used compound. It's a key component in various minerals and construction materials like glass, brick, and concrete, making up about 90% of the Earth's crust. Silicon is prevalent in nanostructures and semiconductor devices, constituting over 99%. Its primary role is as an insulator in silicon-based devices. Recently, there has been a significant increase in the use of silicon dioxide for capturing solar energy. It is widely used in optoelectronic components, including light-emitting diodes and lasers especially in concentrator applications. SiO<sub>2</sub> has a high melting point of 1600 °C [85], allowing it to tolerate high temperatures without melting or deteriorating. SiO<sub>2</sub>'s thermal stability makes it appropriate for use

in high-temperature environments, such as solar thermophotovoltaic systems and optical window applications. In addition, SiO<sub>2</sub>'s low refractive index facilitates the positive coupling of capacitance and inductance, resulting in a broad bandwidth and strong absorption [86]. A standout feature of Silicon Dioxide and its alloys, as materials for photovoltaic cells, is its broad spectrum of design options.

### 3 Design and simulation

The choice of substrate material plays a crucial role in determining the performance of the metamaterial absorber. In this investigation, Silicon Dioxide (SiO<sub>2</sub>) was selected as the substrate due to its effectiveness as a semiconductor in various optoelectronic devices. The SiO<sub>2</sub> substrate offers multiple design possibilities to achieve the desired outcomes. The design and depth of the SiO<sub>2</sub> layer have a significant impact on the efficiency of the metamaterial absorber. In this study, a square-shaped model is proposed, and through a series of trials, it was determined that the optimum absorption rate is achieved with a square substrate having dimensions of 1000 × 1000 nm and a thickness of 160 nm. The layout of the Tungsten resonator is a crucial element in the design of the metamaterial absorber. Metamaterial features emerge when a material interacts

with wavelengths greater than its own. The resonator in this study resembles a flower shape, featuring a ring structure inside, with specific dimensions illustrated in Fig. 1 and Table 1).

The resonator is intentionally designed with visible wavelengths larger than the edge wavelength, enabling effective absorption in the visible range (380–750 nm). The chosen octagonal flower form results in a polarization-insensitive resonator. The thickness of the Tungsten resonator is fixed at 15 nm, a critical factor significantly influencing the absorption rate. For simulation, we utilized CST MWS, employing a frequency-domain solver based on the Finite Integration Technique (FIT) to model the resonator. Both the FIT solver and CST MWS operate on the foundation of the Integral Formulation of Maxwell's Equations. Frequency domain solutions are particularly effective for smaller structures like unit cells and Frequency Selective Surfaces (FSS). The waveguide port's orientation aligns with the x, y, or z axes for accurate evaluation of the blocks. Harmonic equations, in either differential or integral configuration, can be employed to assess the model. In the frequency domain, the finite element technique (FEM) is applied to discretize the surface into triangular elements. Integral equations are also used in phasor representation for these diminutive surfaces. These simulation techniques ensure a comprehensive analysis of the metamaterial resonator's behaviour.

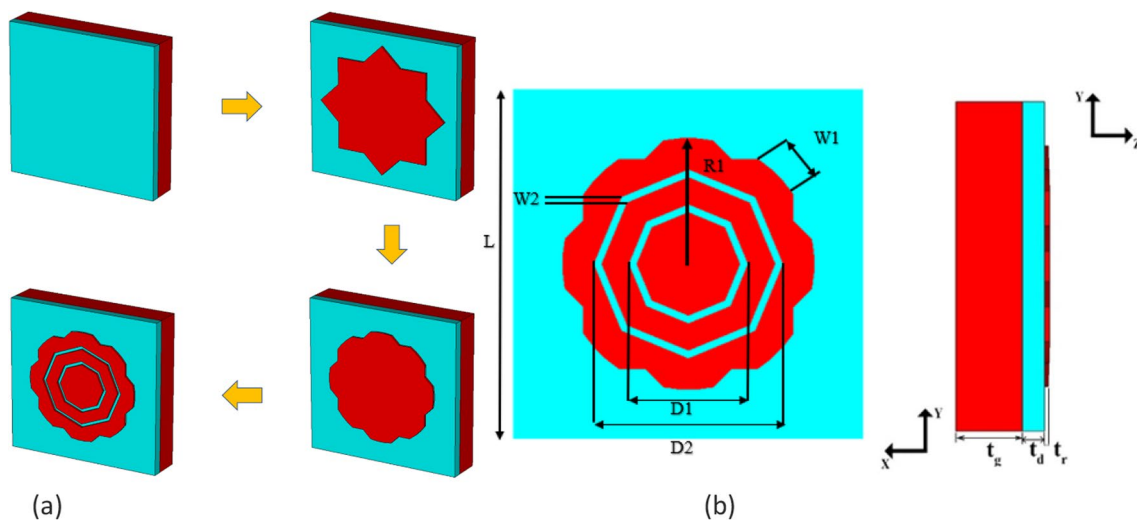


Fig. 1 Demonstration of a design steps of the MMA b front and side view of the MMA with dimension

Table 1 Parameter list of the structure

Parameter	L	tg	td	tr	D1	D2	W2	R1	W1
Value (nm)	1000	160	60	15	340	540	22	360	142.85

### 3.1 Absorption mechanism

The absorption characteristic of a metamaterial absorber depends on some parameter such as  $S_{11}$ ,  $S_{21}$  etc.  $S_{11}$  denotes the coefficient of reflection, while  $S_{21}$  is connected to the coefficient of transmission  $T$  by the equation  $S_{21} = Te^{ik_0d}$  when an incident plane wave strikes a uniform slab with a thickness denoted as ‘td,’ and the coordinate origin is aligned with the initial face of the slab. Using Eqs. (1) and (2)  $S_{11}$  and  $S_{21}$  can be calculated. Here, ‘ $k_0$ ’ represents the wave number of the incoming wave within the open space. Through the linkage of the S parameters with the refractive index ( $n$ ) and impedance ( $z$ ),

$$S_{11} = \frac{R(1 - e^{i2nk_0d})}{1 - R^2 e^{i2nk_0d}} \tag{1}$$

$$S_{21} = \frac{(1 - R^2) e^{ink_0d}}{1 - R^2 * e^{i2nk_0d}} \tag{2}$$

Given  $R = (z-1)/(z+1)$ , it’s worth highlighting that by inverting Eqs. (1) and (2) to solve for the refractive index ‘ $n$ ’ and impedance ‘ $z$ ’, we can consequently derive Eqs. (3) and (4).

$$z = \pm \sqrt{\frac{(1 + S_{11})^2 - S_{21}^2}{(1 - S_{11})^2 - S_{21}^2}} \tag{3}$$

$$e^{inkd} = X \pm i\sqrt{1 - X^2} \tag{4}$$

where  $X = 1/2S_{21}(1 - S_{11}^2 + S_{21}^2)$ .

Our primary goal was to demonstrate that attaining optimal absorption within a designated frequency range requires ascertaining the intrinsic impedance relative to the free space impedance ( $Z_0$ ) of the medium from which the incident wave approaches the structure. The effective permittivity and permeability of the medium are automatically derived from the S parameters, employing Nickolson-ross-Weir equations [87]. The NRW (Numerical Reflectance and Wave Transmission) method utilizes the magnitudes and phases of the reflected and transmitted waves to determine the constitutive parameters. Another calculation method involves using an absorption equation. The absorption value can be derived by leveraging the values of reflection and transmission. These precise measurements are obtained through the utilization of two ports strategically located at the anterior and posterior facets of the absorber configuration. The equation governing absorption is as follows:

$$A(\omega) = 1 - R(\omega) - T(\omega) \tag{5}$$

The goal is to improve absorption. This involves managing both reflection  $R(\omega) = |S_{11}|$  and transmission

$T(\omega) = |S_{21}|$ . Variables in question have a tendency to exhibit frequency-dependent dynamics owing to the dispersive nature of their underlying structure. The transmission  $T(\omega)$  is hindered by a Tungsten plate, seen in Fig. 1b. As a result,  $T(\omega)$  becomes less important, emphasizing the link between the structure’s absorption and  $R(\omega)$ . The analysis of the proposed design follows the absorption equation,

$$A(\omega) = 1 - R(\omega) \tag{6}$$

### 3.2 Result and discussion

In Fig. 2, we can see the absorption and reflectance traits spanning from 400 to 700 nm. These traits pertain to three different modes TEM, TE, and TM. The resonator is made of tungsten, while the dielectric layer is composed of silicon dioxide. These traits stem from Eqs. (1) and (2), using the s-parameter extracted from simulations. This design exhibits remarkable absorption and reflectance characteristics within the optical range across all three modes. The average absorption remains nearly identical for TEM, TE, and TM modes, highlighting the symmetry and quality of the design. The unit cell boasts an average absorption of 97.8% within the optical spectrum. At precisely 540.65 nm, an almost complete absorption peak (99.99%) manifests for all three modes. The designed absorber showcases exceptional potential in capturing solar energy throughout the day, with an efficiency of up to 9%. This performance surpasses semiconductor absorbers that suffer from energy losses. From the figure depicted in Fig. 2, it

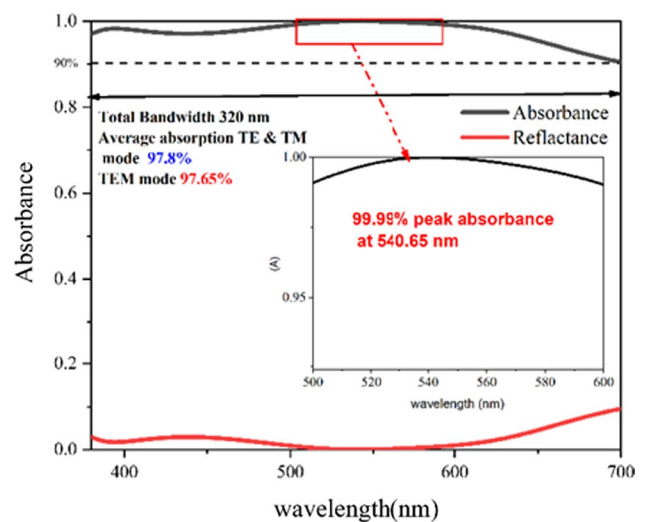


Fig. 2 Demonstration of the proposed absorber’s absorption and reflection pointing the resonance point

can be seen that at point 540.65 nm the resonance point occurs and thus the maximum peak absorption occurs. At this point the electron of the structure vibrates.

### 3.3 Co-polarization and cross-polarization

As observed earlier, the curve of absorption is derived using Eqs. (5) and (6). Nevertheless, when employing an MMA, a pertinent query arises: Does the unit cell operate as a polarization converter, resulting in the PCR value instead of absorption. Despite the symmetrical nature of the structure, we harnessed Eqs. (7) and (8) to illustrate both co-polarization and cross-polarization constituents in Fig. 3. The negligible presence of the cross-polarization component on the linear magnitude scale in Fig. 3 indicates that the design refrains from altering waves within the wavelength span under examination.

$$|S_{11}|^2 = |R_{yy}|^2 + |R_{yx}|^2 \tag{7}$$

$$|S_{11}|^2 = |R_{xx}|^2 + |R_{xy}|^2 \tag{8}$$

$$PCR_{TE} = \frac{(R_{yx})^2}{(R_{yy})^2 + R_{yx}^2} \tag{9}$$

$$PCR_{TM} = \frac{R_{xy}^2}{(R_{xx}^2 + R_{xy}^2)} \tag{10}$$

In this scenario,  $R_{yy}$  and  $R_{xx}$  represent the reflectivity related to co-polarization, while  $R_{yx}$  and  $R_{xy}$  are the reflectivity associated with cross-polarization [88, 89]. Additionally, the PCR (polarization conversion ratio) for the unit cell can be calculated using Eqs. (9) or (10), as depicted in Fig. 3(b). From figure it is evident that even the maximum point of the PCR value is below 0.03. The PCR value for the proposed design approaches zero for both TE and TM modes, effectively eradicating any concerns about polarization conversion traits.

Incident angle simulation for metamaterial absorbers is necessary to study their performance and effectiveness under different polarization conditions. The incident angle refers to the angle at which the wave approaches the absorber’s surface. Incident angle simulation for metamaterial absorbers is essential for assessing their absorption characteristics under different incident wave angles and polarization states. In the case of incident angle and polarization, metamaterial absorbers are often designed to operate efficiently for specific polarizations and limited incident angles. However, the real-world environment may introduce incident waves with different polarization states. By simulating various polarization conditions, researchers can evaluate the absorber’s performance and determine if it can be effective. The absorption characteristics of the devised absorber were additionally assessed through a visual representation of the angle of polarization. This portrayal can be observed in Fig. 4(a) and (b).

The stability of the incident angle is also assessed, as depicted in Fig. 4(c) and (d). This evaluation encompasses both TE and TM modes, investigating polarization across angles from 0° to 70°. Suggested design showcases

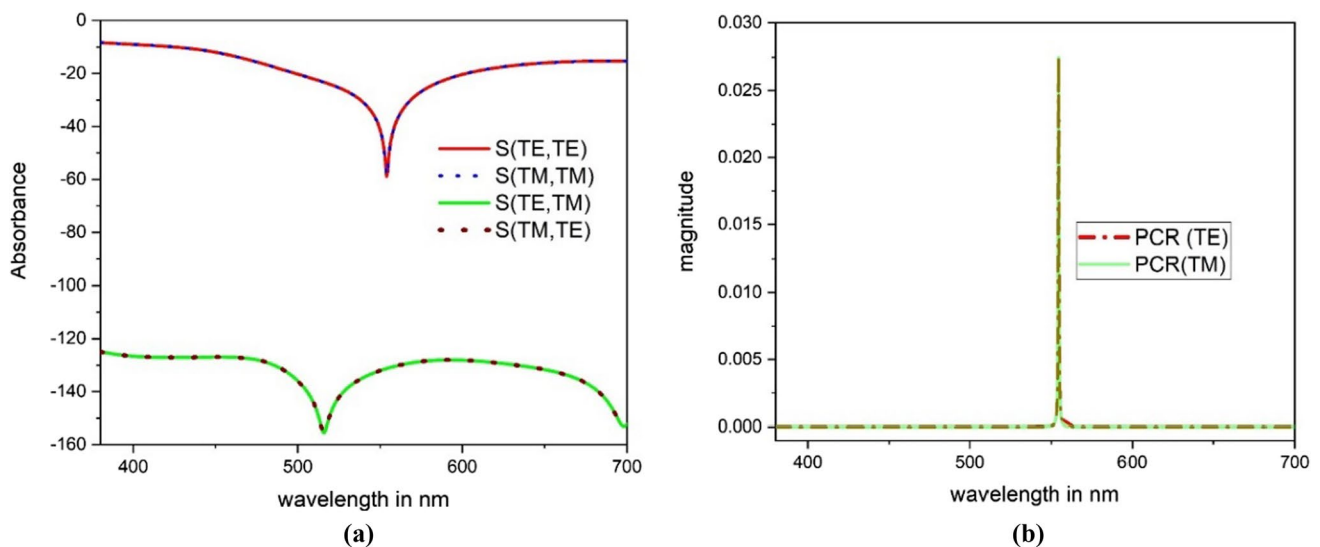


**Fig. 3** **a** The unit cell’s behaviour in terms of co-polarization and cross-polarization. **b** The Polarization Conversion Ratio (PCR) for the designed unit cell, assessed in both TE and TM modes

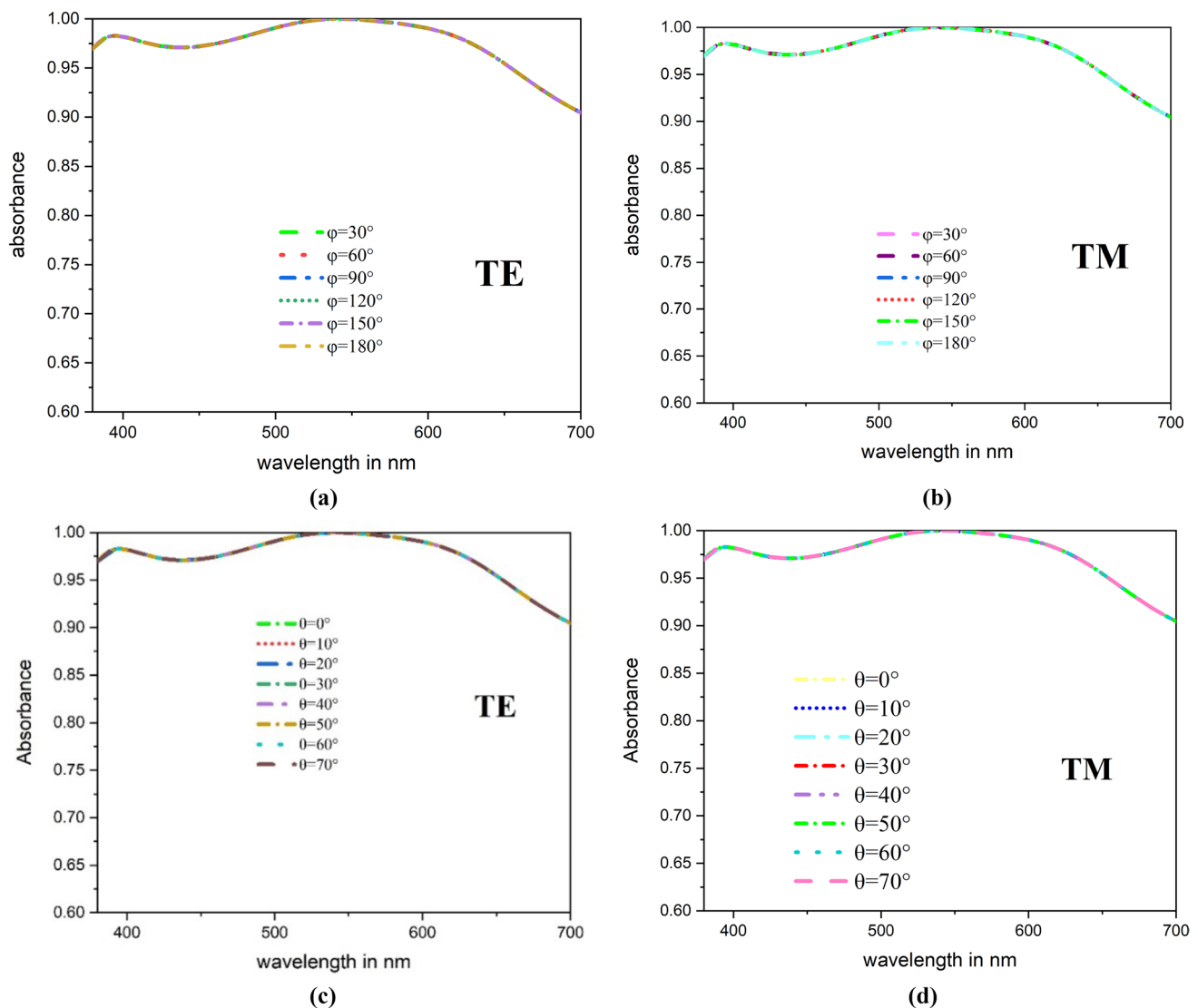


**Fig. 4** The Illustration of alterations in the angle of polarization angle for **a** TE mode and **b** TM mode, as well as variations in the incident angle for **c** TE mode and **d** TM mode

exceptional absorption qualities that remain consistent across both TE and TM modes, spanning a range of incident EM wave polarization angles from  $0^\circ$  to  $70^\circ$  with increments of  $10^\circ$ . Whether the angle is in all the polarization mode it does not affect the absorption property of the metamaterial. The average remain 97.8% in all mode and the peak is 99.99% at 54.65 nm.

### 3.4 Geometric sweep

The parameters wield considerable influence over the geometric configuration, with the geometric structure in turn exerting a substantial impact on absorption. The crucial parameter exploration is elucidated, as demonstrated in Fig. 5. Notably, a significant fluctuation manifested during

alterations in dielectric thickness ( $t_d$ ), evident in Fig. 5(a). In recent previous research, the thickness varied from 60 to 150 nm [90–92]. Inspired by these thickness values, we selected an optimized dielectric thickness of 60 nm. A significant change in absorbance was observed when transitioning from 50 to 70 nm thicknesses, leading to a red shift in absorbance. Specifically, resonance readings of 99.3%, 99.88%, 99.99%, 99.95%, and 99.76% were recorded for dielectric layer thicknesses of 50, 55, 60, 65, and 70 nm respectively. These resonant wavelengths experienced linear shifts in response to changes in dielectric layer thickness, settling at 496.8, 515.8, 564, 540.65, 672.85, and 602 nm, respectively. Peak absorption gradually increases as the dielectric thickness increase but start to reduce for further increase. Moreover, the resonant point shifts from left to

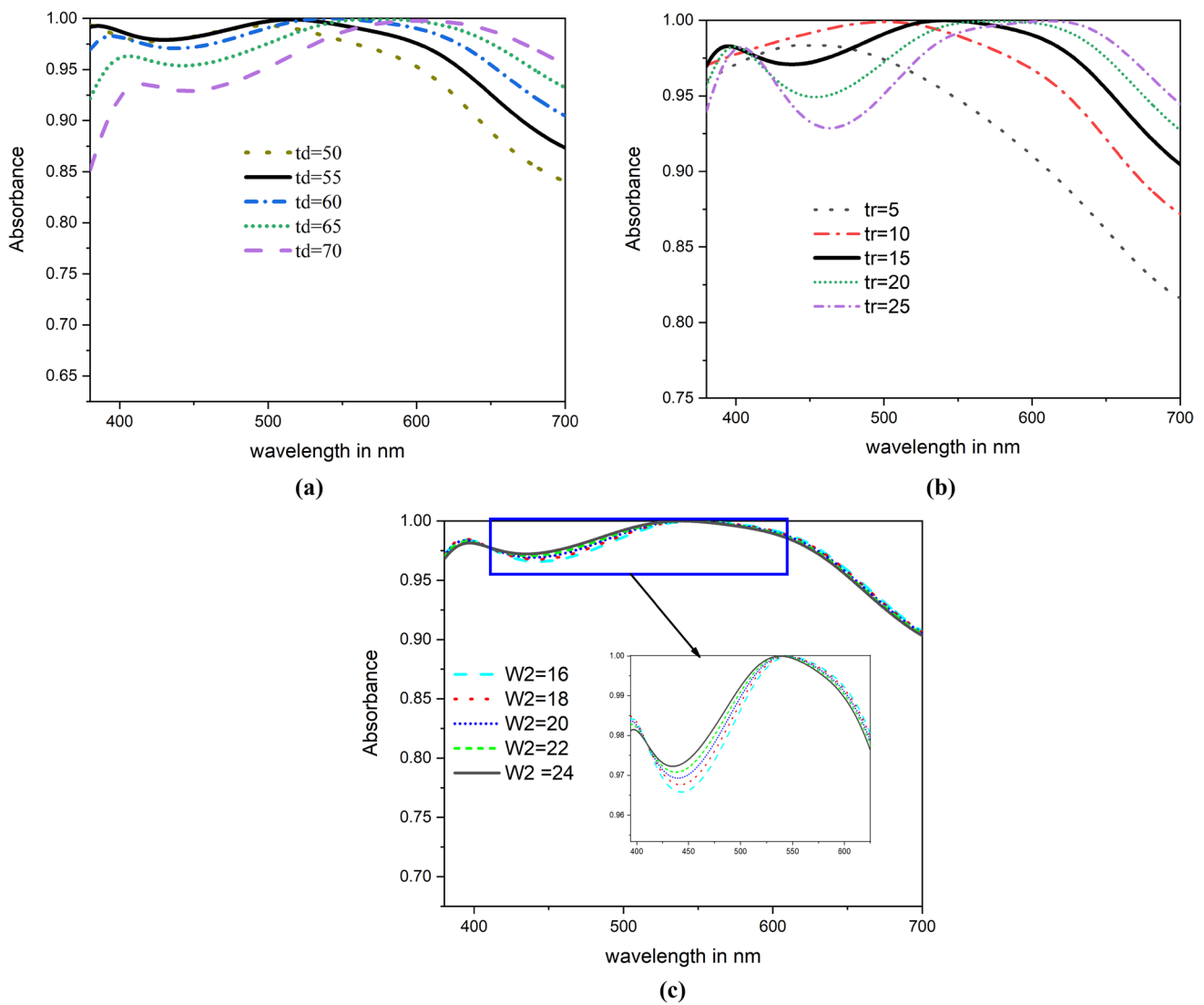


**Fig. 5** Change of **a** dielectric thickness **b** resonator thickness and **c** change of W2

right for dielectric thickness changes that is described visually in the figure mentioned.

The increase in the thickness of the dielectric insulator influences the current flow in the ground layer and the inductance of the meta-structure [93]. In simple, when the dielectric thickness is increased, the meta-structure absorbs longer wavelengths in the electromagnetic spectrum. This is evident in the proposed metamaterial absorber’s absorbance characteristic, specifically in the range of 420–500 nm. As the thickness increases, the absorption peak shifts towards longer wavelengths. This shift represents the blue shift which is caused by coupling that occurs between the resonator and bottom plate [94]. Conversely, elevating absorption peaks is challenging with a small dielectric thickness [95]. Controlling the thickness of the spacer in metamaterial absorbers allows for

the manipulation of total reflection; achieving anti-phased reflections with equal amplitudes at a critical spacer thickness leads to destructive interference, ultimately resulting in perfect absorption of the incident waves[96]. Therefore, the optimized value of dielectric layer was chosen 60 nm as the impedance matched at this value perfectly. The thickness of the resonator (tr) is systematically varied between 5 and 25 nm, with an incremental step of 5 nm. The outcomes of this variation are elucidated in Fig. 5(b). Notably, the resonant absorption experiences an upward trajectory with the expanding thickness until it reaches 15 nm, beyond which it undergoes a decline. This shift is attributed to the influence of resonator thickness on achieving an optimal match with the free-space impedance. The structure is created with a thickness of 15 nm to get the optimum impedance matching.

The resonant absorption is 98.2%, 99.90%, 99.99%, 99.37%, and 99.25% for different “tr” values such as 5, 10, 15, 20, 25 nm. Parameter ‘W2’ changed from, 16 nm to 24 nm with an increment of 2 nm. Figure 5 (c) represents that the absorption for changing the gap width “W2” from 16 to 24 nm does not affect much.

### 3.5 Absorption with different dielectric and resonator

Our chosen substrate is silicon dioxide (SiO<sub>2</sub>). However, it’s important to analyze the effects of using different materials for both dielectric and metal components. Using a dielectric material that was altered, we conducted an analysis. A comprehensive study was conducted to explore how meta-material absorbers perform with varying substrate and metal materials. We evaluated four materials as substrates: aluminum nitride, gallium arsenide (GaAs), amorphous silicon (a-Si), and silicon nitride (Si<sub>3</sub>N<sub>4</sub>).

Figure 6(a) shows a progressive rise in absorption for silicon nitride, accompanied by a movement to the left in the resonant point. Notably, the maximum peak absorption of 99.98% occurs at 674.2 nm. However, this increase in peak absorption is offset by a decrease in overall absorption rate. Gallium Arsenide, on the other hand, has lower absorption levels than the others, whereas amorphous silicon has around half the absorption throughout the full wavelength range. Moving on to Fig. 6(b), we investigate the absorption characteristics of several metals. This research focuses on five metals: aluminum, copper, gold, platinum, and tin. Surprisingly, two nearly-perfect absorption peaks appear at 400 nm and 570 nm, respectively, with absorption

rates of 99.998% and 99.9978%. Another prominent peak at 624.56 nm has a 98% absorption rate.

From the figure and previously done analysis it is evident that tungsten possesses high efficiency rather than other material. The broadband high absorption of tungsten is attributed to its high intrinsic loss, along with the presence of surface plasmon polaritons and magnetic polaritons [97]. The primary benefit of utilizing tungsten lies in its ability to amplify light absorption within the spectrum’s shorter wavelengths [82]. In addition the substantial real component of its dielectric constant, tungsten exhibits a high reflectance of light in the infrared spectrum but a high absorbance of light in the visible spectrum [84]. Hence, due to its favorable impedance match in free space and minimal ohmic

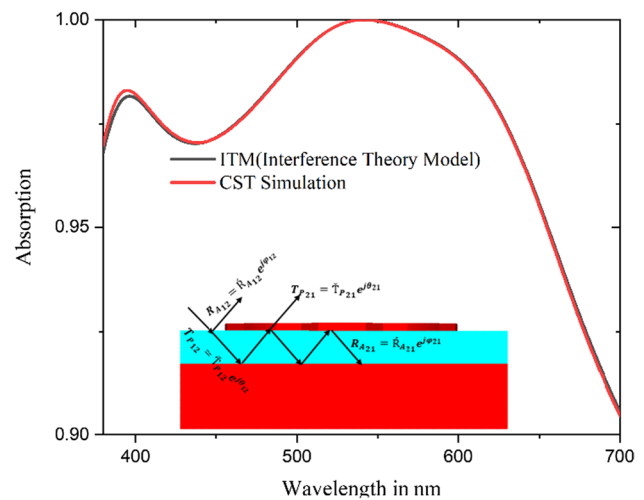


Fig. 7 Comparison of absorption obtained interference theory and simulation

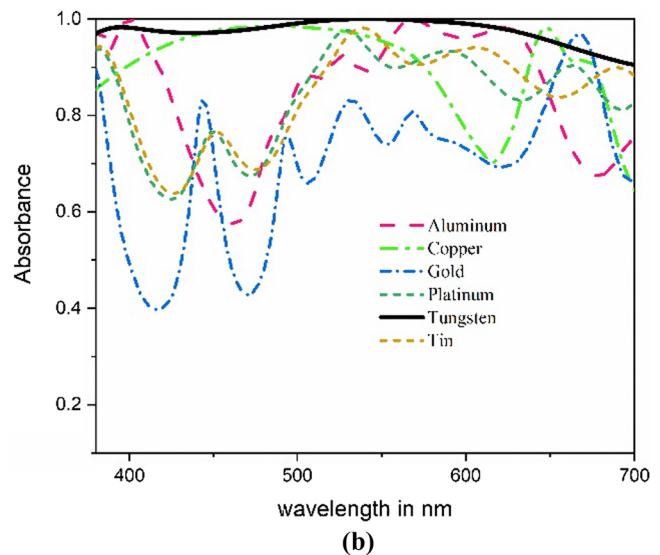
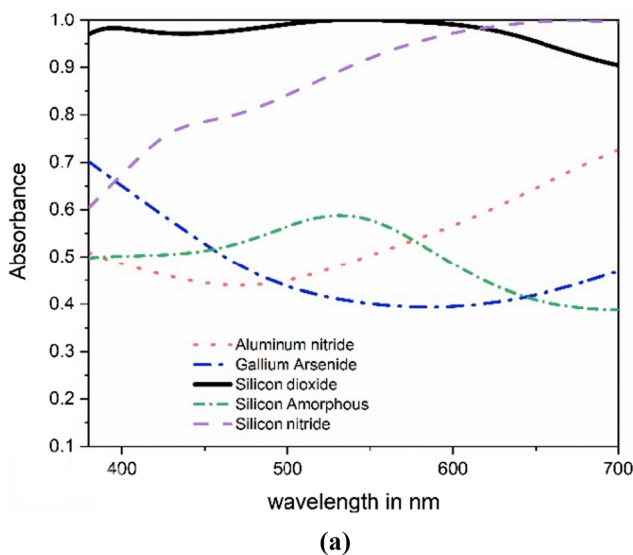


Fig. 6 Analysis of the absorption utilizing various a resonator layer material and b dielectric layer’s material



losses and the unique features mentioned tungsten exhibits improved absorption.

### 3.6 Validation the MMA with interference theory

Using the interference theory, the absorption mechanism can be explaining also this theory can validate the absorption efficiency. As indicated in the inset to Fig. 7, at the air-spacer interface with the cross-resonator array, a portion of the incident electromagnetic wave is partially reflected back to the air with a reflection coefficient  $R_{A12} = R_{A12}e^{j\varphi_{12}}$  the other part of Em wave propagate inside the dielectric layer with coefficient  $T_{P12} = R_{P12}e^{j\varphi_{12}}$ . The transmitted light continues to propagate until it reaches the ground plane. This transmitted wave propagates with a complex propagation phase  $\beta = \beta_p + i\beta_M = \sqrt{\epsilon_d}K_0d$  where  $\beta_p$  is the propagation phase and  $\beta_M$  represents absorption happens in dielectric. Free space wave number

is denoted as  $K_0$  and  $d$  is the propagation distance. The transmitted wave reflects back at the bottom metal layer, and partial reflection and transmission occur at the adjacent region of the resonator and dielectric with a reflection coefficient.  $R_{A12} = R_{A12}e^{j\varphi_{12}}$  and transmission coefficient  $T_{P12} = T_{P12}e^{j\varphi_{21}}$ . The total reflection is the outcome of the superposition of multiple reflections and can be expressed as below [98],

$$R_T = R_{A12} - \frac{T_{P12}T_{P21}e^{j2\beta}}{1 + R_{A21}e^{j2\beta}} \tag{11}$$

The graph obtained from the calculations is illustrated in Fig. 7, where the simulation results are compared with those obtained from interference theory. The average absorption achieved from simulation is 97.8%, while the result extracted by the Interference Theory Model (ITM)

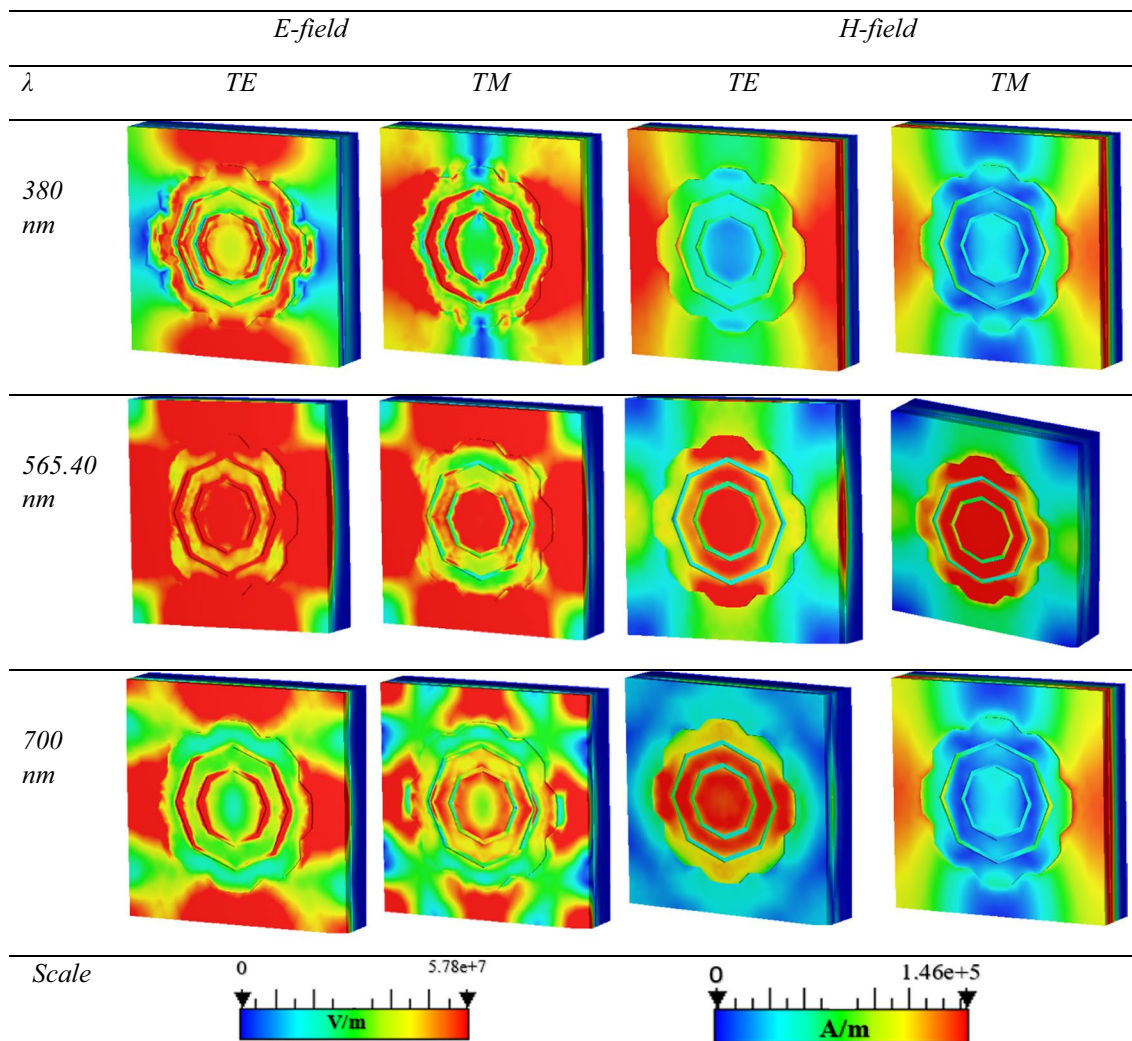


Fig. 8 Demonstration of E field and H-field distribution at different wavelength including resonant point

attains an average of 97.64%, indicating a nearly identical match between the two.

### 3.7 E-field and H-field

The absorption process can also be explained by the E-field (Electric field) and the distribution of the magnetic field H at the resonant frequency. The absolute value of the electric E-field is shown in Fig. 8 for the electromagnetic field at a wavelength of 540.65 nm (resonance). In Fig. 8, the E-field is largely located from the external surface of the resonator to half of the center, including the corner space of the flower-shaped resonator, and it is greatest at the resonance value of 540.65 nm. Figure 8 shows a strong E-field for both TE and TM modes with wavelengths above. This is one of the most important reasons for the high absorption discussed previously.

The magnetic field exhibited in Fig. 8 for wavelengths of 380 nm, 565.4 nm, and 700 nm in both modes, like the E-field. Similar to the dependable and widespread E-field, the design exhibits a highly effective vast H-field. This characteristic propelled the structure towards achieving an excellent polarization-independent MMA across the entire optical spectrum.

In the previously presented absorption figure, a dip is noticeable in the range of 420–500 nm, attributed to the inefficient formation of resonance. To gain a comprehensive understanding of the absorption behavior within this wavelength range, we conducted demonstrations of the E-field and H-field distributions for 450 nm (refer to Fig. 9). The electric field distribution at this wavelength indicates a low resonance, which is the contributing factor to the reduced absorption of the proposed Metamaterial Absorber (MMA). Only a small localized surface plasmon resonance occurs at the upper and lower sides of the structure and the surrounding area of the resonator. The figure illustrates that, in this region, a low magnetic field distribution is formed throughout the structure. At a wavelength of 450 nm, the

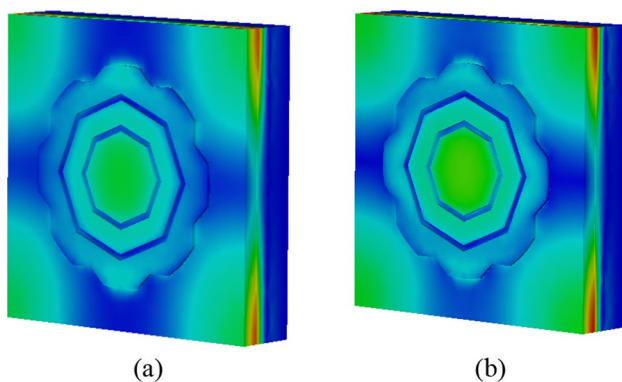


**Fig. 9** Distribution of **a** E-field and **b** H-field wavelength 450 nm

maximum resonance occurs in the lower dielectric layer, with low resonance on the surface of that layer. This observation suggests that propagation plasmon resonance is happening in that region. Conversely, low localized plasmon resonance occurs at the central resonator surface. Thus, at this wavelength, low resonance is responsible for the dip observed in the absorption curve. In the case of absorption, the E-field and H-field cause currents in the metamaterial, which, in turn, create an opposing electromagnetic wave. This conflicting wave interacts with the incoming wave, leading to detrimental interference and the absorption of energy. The metamaterials' resonant characteristic allows them to link with the incident electromagnetic wave, increasing absorption efficiency. Absorption may be improved for specific or desired frequencies by changing the structural and compositional landmark of the metamaterial. Overall, E-field and H-field interactions with metamaterials enable electromagnetic energy absorption by using resonant characteristics and creating opposing waves via induced currents. This absorption property has a vast range of uses, including harvesting the energy, sensing, and electromagnetic wave manipulation.

### 3.8 Comparative analysis

In this section, a comparison is made between the proposed metamaterial absorber (MMA) and comparable structures from recent studies encompassing the optical region. This MMA's design distinguishes out in various ways, providing higher performance when compared to others. It has an ultrathin layer made of materials with improved temperature stability, which is critical for solar spectrum functioning. Furthermore, the materials employed in this design are less expensive than alternatives such as gold or silicon. The MMA performs well at incidence angles of up to 70 degrees, making it ideal for energy harvesting and sensing applications. Another benefit is the use of tungsten as the base metal, which eliminates the requirement for quartz or glass layers and lowers production costs. This suggested MMA is a great option for a variety of optical area applications because to its wide bandwidth of about 320 nm, exceptional 99.999% absorption peak, and the aforementioned characteristics that can be easily seen from Table 2.

## 4 Conclusion

In this study, a noteworthy achievement has been made with the design of an extremely broadband metamaterial absorber (MMA) tailored for visible wavelengths spanning from 380 to 700 nm, corresponding to an impressive frequency range of 400THz to 780THz. Utilizing tungsten and silicon dioxide material the most common

**Table 2** Comparison between previous work

Ref	Layer	Size	Bandwidth	Material used	Polarisation and angular sensitivity	Peak value	Average absorption
[21]	Three	200×200×125	350	W, SiO <sub>2</sub>	No, < 60°	99%	90%
[31]	Three	1000×1000×225	308	W, SiO <sub>2</sub>	Yes < 60°	99.99%	96.77
[76]	Three	900×900×197.8	370	W, SiO <sub>2</sub>	Yes < 70°	99.99%	97%
[99]	Periodic array	500×500×600	310	Au, Si	Yes < 65°	98.5%	90%
[100]	Four	Periodic×350	300	Cu, Si <sub>3</sub> N <sub>4</sub> ,Si	NO, not available	97%	90%
[101]	Three	380×380×235	300	Ag, SiO <sub>2</sub>	Yes < 60°	98	70%
[102]	Four	Nanocomposite with width = 250	350	SiO <sub>2</sub> -Au composite, SiO <sub>2</sub> ,Au,glass	Yes < 60°	99	N/A
[103]	Three	250×250×355	300	Ni, Si	Yes < 60°	99%	90%
[104]	Three	350×350×180	300	Ag, SiO <sub>2</sub>	No. N/A	98%	90%
[105]	Three	520×520×180	219	Ni, Rexolite (PS) W	No	99.74%	N/A
Proposed	Three	1000×1000×225	320	W, SiO <sub>2</sub>	Yes < 70°	99.999%	97.8%

method used here is a sandwich-type three-layer arrangement that includes a metal-dielectric-metal layer. The resultant MMA has a wide bandwidth, with near-perfect absorption surpassing 90.28% over the spectrum. It also has a fascinating feature known as angular independence, which ensures consistent and strong absorption performance independent of incidence angle. As seen in Fig. 6, the use of lossy Silicon Dioxide (SiO<sub>2</sub>) in our simulations increases the importance of this work. Furthermore, intensive research involving four different dielectric materials has given a variety of still important results, as shown in figure.

Even though we were unable to create the MA during this study project, we predict that the measured values will closely match the projected outcomes. Future practical implementations have the potential to validate our findings. Notably, the MMA's angular independence makes it well-suited for solar energy harvesting applications, with its outstanding absorption of 99.999% and average absorption of 97.8% potentially increasing the efficiency of solar panels. Furthermore, the MA might be used as a half-power absorber by including Silicon Amorphous, Gallium Arsenide, or Aluminum nitride. Meanwhile, the inclusion of Silicon Nitride (Si<sub>3</sub>N<sub>4</sub>) extends the wavelength range, potentially opening up uses as a light wavelength detector.

**Author contributions** Conceptualization, formal analysis, investigation, methodology, writing-original draft, M.R.; formal analysis, result investigation, review, S.S.I; final review and editing A.R.S

**Data availability** The data presented in this study are presented in this article.

## Declarations

**Conflict of interest** The authors declare no conflict of interest.

## References

- V.G. Veselago, Reviews of topical problems: the electrodynamics of substances with simultaneously negative values of  $\epsilon$  and  $\mu$ . *Soviet Phys. Uspekhi* **10**(4), R04 (1968)
- R.S. Kshetrimayum, A brief intro to metamaterials. *IEEE Potentials* **23**(5), 44–46 (2004)
- D. Schurig, J. Mock, D. Smith, Electric-field-coupled resonators for negative permittivity metamaterials. *Appl. Phys. Lett.* (2006). <https://doi.org/10.1063/1.2166681>
- B. Li, G. Sui, W.H. Zhong, Single negative metamaterials in unstructured polymer nanocomposites toward selectable and controllable negative permittivity. *Adv. Mater.* **21**(41), 4176–4180 (2009)
- N. Engheta, An idea for thin subwavelength cavity resonators using metamaterials with negative permittivity and permeability. *IEEE Antennas Wirel. Propag. Lett.* **1**, 10–13 (2002)
- R. Marqués, F. Medina, R. Rafii-El-Idrissi, Role of bianisotropy in negative permeability and left-handed metamaterials. *Phys. Rev. B* **65**(14), 144440 (2002)
- W.J. Padilla, D.N. Basov, D.R. Smith, Negative refractive index metamaterials. *Mater. Today* **9**(7–8), 28–35 (2006)
- J. Zeng, X. Wang, J. Sun, A. Pandey, A.N. Cartwright, N.M. Litchinitser, Manipulating complex light with metamaterials. *Sci. Rep.* **3**(1), 2826 (2013)
- G. Lipworth et al., Magnetic metamaterial superlens for increased range wireless power transfer. *Sci. Rep.* **4**(1), 3642 (2014)
- N. Fang, X. Zhang, "Imaging properties of a metamaterial superlens," in *Proceedings of the 2nd IEEE Conference on Nanotechnology*. IEEE, pp. 225–228 (2002)
- S.S. Islam, M.R.I. Faruque, M.T. Islam, An object-independent ENZ metamaterial-based wideband electromagnetic cloak. *Sci. Rep.* **6**(1), 1–10 (2016)
- B. Kanté, D. Germain, A. de Lustrac, Experimental demonstration of a nonmagnetic metamaterial cloak at microwave frequencies. *Phys. Rev. B* **80**(20), 201104 (2009)
- Y. Wang et al., Triple-band perfect metamaterial absorber with good operating angle polarization tolerance based on split ring arrays. *Results Phys.* **16**, 102951 (2020)
- N.I. Landy, S. Sajuyigbe, J.J. Mock, D.R. Smith, W.J. Padilla, Perfect metamaterial absorber. *Phys. Rev. Lett.* **100**(20), 207402 (2008)

15. C. Cen et al., Theoretical design of a triple-band perfect metamaterial absorber in the THz frequency range. *Results Phys.* **14**, 102463 (2019)
16. M.R.I. Faruque, E. Ahamed, M.A. Rahman, M.T. Islam, Flexible nickel aluminate (NiAl<sub>2</sub>O<sub>4</sub>) based dual-band double negative metamaterial for microwave applications. *Results Phys.* **14**, 102524 (2019)
17. T.M. Hossain, M.F. Jamlos, M.A. Jamlos, P.J. Soh, M.I. Islam, R. Khan, Modified H-shaped DNG metamaterial for multiband microwave application. *Appl. Phys. A* **124**, 1–7 (2018)
18. A.M. Tamim, M.R.I. Faruque, M.J. Alam, S.S. Islam, M.T. Islam, Split ring resonator loaded horizontally inverse double L-shaped metamaterial for C-, X-and Ku-Band Microwave applications. *Results Phys.* **12**, 2112–2122 (2019)
19. H.-T. Chen, W.J. Padilla, J.M. Zide, A.C. Gossard, A.J. Taylor, R.D. Averitt, Active terahertz metamaterial devices. *Nature* **444**(7119), 597–600 (2006)
20. H.-E. Su, J.-L. Li, L. Xia, A novel temperature controlled broadband metamaterial absorber for THz applications. *IEEE Access* **7**, 161255–161263 (2019)
21. R. Bilal et al., Elliptical metallic rings-shaped fractal metamaterial absorber in the visible regime. *Sci. Rep.* **10**(1), 1–12 (2020)
22. S. Mahmud, S.S. Islam, A.F. Almutairi, M.T. Islam, A wide incident angle, ultrathin, polarization-insensitive metamaterial absorber for optical wavelength applications. *IEEE Access* **8**, 129525–129541 (2020)
23. S. Mahmud et al., A multi-band near perfect polarization and angular insensitive metamaterial absorber with a simple octagonal resonator for visible wavelength. *IEEE Access* **9**, 117746–117760 (2021)
24. T. Chen, S. Li, H. Sun, Metamaterials application in sensing. *Sensors* **12**(3), 2742–2765 (2012)
25. A. Tamer et al., Metamaterial based sensor integrating transmission line for detection of branded and unbranded diesel fuel. *Chem. Phys. Lett.* **742**, 137169 (2020)
26. Y.I. Abdulkarim et al., Design and study of a metamaterial based sensor for the application of liquid chemicals detection. *J. Market. Res.* **9**(5), 10291–10304 (2020)
27. W.J. Padilla, R.D. Averitt, Imaging with metamaterials. *Nat. Rev. Phys.* **4**(2), 85–100 (2022)
28. G. Lipworth et al., Comprehensive simulation platform for a metamaterial imaging system. *Appl. Opt.* **54**(31), 9343–9353 (2015)
29. D. Shrekenhamer, W. Xu, S. Venkatesh, D. Schurig, S. Sonkusale, W.J. Padilla, Experimental realization of a metamaterial detector focal plane array. *Phys. Rev. Lett.* **109**(17), 177401 (2012)
30. M.M. Hassan, F.S. Sium, F. Islam, S.M. Choudhury, A review on plasmonic and metamaterial based biosensing platforms for virus detection. *Sensing Bio-Sensing Res.* **33**, 100429 (2021)
31. S. Mahmud, S.S. Islam, K. Mat, M.E. Chowdhury, H. Rmili, M.T. Islam, Design and parametric analysis of a wide-angle polarization-insensitive metamaterial absorber with a star shape resonator for optical wavelength applications. *Results Phys.* **18**, 103259 (2020)
32. Z.-Q. Lu, L. Zhao, H. Ding, L.-Q. Chen, A dual-functional metamaterial for integrated vibration isolation and energy harvesting. *J. Sound Vib.* **509**, 116251 (2021)
33. M.B. Hossain, M.R.I. Faruque, S.S. Islam, M.T. Islam, Modified double dumbbell-shaped split-ring resonator-based negative permittivity metamaterial for satellite communications with high effective medium ratio. *Sci. Rep.* **11**(1), 19331 (2021)
34. M.R. Islam et al., Square enclosed circle split ring resonator enabled epsilon negative (ENG) near zero index (NZI) metamaterial for gain enhancement of multiband satellite and radar antenna applications. *Results Phys.* **19**, 103556 (2020)
35. M.T. Islam, M. Cho, M. Samsuzzaman, S. Kibria, Compact antenna for small satellite applications [Antenna Applications Corner]. *IEEE Antennas Propag. Mag.* **57**(2), 30–36 (2015)
36. M. Islam, M.T. Islam, M. Samsuzzaman, M.R.I. Faruque, Compact metamaterial antenna for UWB applications. *Electron. Lett.* **51**(16), 1222–1224 (2015)
37. M.H. Habaebi, M. Janat, M.R. Islam, B. Hamida, "Phased array antenna metamaterial based design operating in millimeter wave for 5G mobile networks," in 2016 IEEE Student Conference on Research and Development (SCoReD), IEEE, pp. 1–4 (2016)
38. T. Shabbir, R. Saleem, S.S. Al-Bawri, M.F. Shafique, M.T. Islam, Eight-port metamaterial loaded UWB-MIMO antenna system for 3D system-in-package applications. *IEEE Access* **8**, 106982–106992 (2020)
39. R.W. Ziolkowski, P. Jin, C.-C. Lin, Metamaterial-inspired engineering of antennas. *Proc. IEEE* **99**(10), 1720–1731 (2010)
40. R. Azim, M.T. Islam, A.T. Mobashsher, Design of a dual band-notch UWB slot antenna by means of simple parasitic slits. *IEEE Antennas Wirel. Propag. Lett.* **12**, 1412–1415 (2013)
41. M.S. Alam, N. Misran, B. Yatim, and M. T. Islam, Development of electromagnetic band gap structures in the perspective of microstrip antenna design, *Int. J. Antennas Propag* (2013)
42. R. Azim, M.T. Islam, N. Misran, S. Cheung, Y. Yamada, Planar UWB antenna with multi-slotted ground plane. *Microw. Opt. Technol. Lett.* **53**(5), 966–968 (2011)
43. J. Tiang, M. Islam, N. Misran, J. Mandeep, Slot loaded circular microstrip antenna with meandered slits. *J. Electromagn. Waves Appl.* **25**(13), 1851–1862 (2011)
44. N. Alrayes, M.I. Hussein, Metamaterial-based sensor design using split ring resonator and Hilbert fractal for biomedical application. *Sensing Bio-Sensing Res.* **31**, 100395 (2021)
45. R.K. Pokharel, A. Barakat, S. Alshhawy, K. Yoshitomi, C. Saris, Wireless power transfer system rigid to tissue characteristics using metamaterial inspired geometry for biomedical implant applications. *Sci. Rep.* **11**(1), 5868 (2021)
46. C. Enkrich et al., Magnetic metamaterials at telecommunication and visible frequencies. *Phys. Rev. Lett.* **95**(20), 203901 (2005)
47. M. AbuHussain, U.C. Hasar, Design of X-bandpass waveguide Chebyshev filter based on CSRR metamaterial for telecommunication systems. *Electronics* **9**(1), 101 (2020)
48. G. Dolling, C. Enkrich, M. Wegener, C.M. Soukoulis, S. Linden, Low-loss negative-index metamaterial at telecommunication wavelengths. *Opt. Lett.* **31**(12), 1800–1802 (2006)
49. A.S. Dhillon, D. Mittal, R. Bargota, Triple band ultrathin polarization insensitive metamaterial absorber for defense, explosive detection and airborne radar applications. *Microw. Opt. Technol. Lett.* **61**(1), 89–95 (2019)
50. Y. Liu, Y. Hao, K. Li, S. Gong, Radar cross section reduction of a microstrip antenna based on polarization conversion metamaterial. *IEEE Antennas Wirel. Propag. Lett.* **15**, 80–83 (2015)
51. S.A. Cummer, J. Christensen, A. Alù, Controlling sound with acoustic metamaterials. *Nat. Rev. Mater.* **1**(3), 1–13 (2016)
52. R.L. Harne, Y. Song, Q. Dai, Trapping and attenuating broadband vibroacoustic energy with hyperdamping metamaterials. *Extreme Mech. Lett.* **12**, 41–47 (2017)
53. S. Zhang, L. Yin, N. Fang, Focusing ultrasound with an acoustic metamaterial network. *Phys. Rev. Lett.* **102**(19), 194301 (2009)
54. J.-Y. Jang, C.-S. Park, K. Song, Lightweight soundproofing membrane acoustic metamaterial for broadband sound insulation. *Mech. Syst. Signal Process.* **178**, 109270 (2022)
55. J.W. Jung, J.E. Kim, J.W. Lee, Acoustic metamaterial panel for both fluid passage and broadband soundproofing in the audible frequency range. *Appl. Phys. Lett.* **112**(4), 041903 (2018)
56. S. Haxha, F. AbdelMalek, F. Ouerghi, M. Charlton, A. Aggoun, X. Fang, Metamaterial superlenses operating at visible wavelength for imaging applications. *Sci. Rep.* **8**(1), 16119 (2018)

- 57 K. Aydin, I. Bulu, E. Ozbay, Subwavelength resolution with a negative-index metamaterial superlens. *Appl. Phys. Lett.* (2007). <https://doi.org/10.1063/1.2750393>
- 58 X. Zhang, Z. Liu, Superlenses to overcome the diffraction limit. *Nat. Mater.* **7**(6), 435–441 (2008)
- 59 R.K. Mishra, R.D. Gupta, S. Datar, Metamaterial microwave absorber (MMA) for electromagnetic interference (EMI) shielding in X-band. *Plasmonics* **16**(6), 2061–2071 (2021)
- 60 M. Jaroszewski, S. Thomas, and A. V. Rane, Advanced materials for electromagnetic shielding: fundamentals, properties, and applications (2018)
- 61 A. Rahman, M.T. Islam, M.J. Singh, S. Kibria, M. Akhtaruzzaman, Electromagnetic performances analysis of an ultra-wideband and flexible material antenna in microwave breast imaging: To implement a wearable medical bra. *Sci. Rep.* **6**(1), 38906 (2016)
- 62 M.Z. Mahmud, M.T. Islam, N. Misran, S. Kibria, M. Samsuzzaman, Microwave imaging for breast tumor detection using uniplanar AMC based CPW-fed microstrip antenna. *IEEE Access* **6**, 44763–44775 (2018)
- 63 M.T. Islam, M. Samsuzzaman, M.T. Islam, S. Kibria, M.J. Singh, A homogeneous breast phantom measurement system with an improved modified microwave imaging antenna sensor. *Sensors* **18**(9), 2962 (2018)
- 64 M. Rokunuzzaman, M. Samsuzzaman, M.T. Islam, Unidirectional wideband 3-D antenna for human head-imaging application. *IEEE Antennas Wirel. Propag. Lett.* **16**, 169–172 (2016)
- 65 J.C. Song, N.M. Gabor, Electron quantum metamaterials in van der Waals heterostructures. *Nat. Nanotechnol.* **13**(11), 986–993 (2018)
- 66 A.M. Zagoskin, D. Felbacq, E. Rousseau, Quantum metamaterials in the microwave and optical ranges. *EPJ Quantum Technol.* **3**(1), 1–17 (2016)
- 67 A. Afridi, S. Ullah, S. Khan, A. Ahmed, A.H. Khalil, M.A. Tarar, Design of dual band wearable antenna using metamaterials. *J. Microw. Power Electromagn. Energy.* **47**(2), 126–137 (2013)
- 68 S. Il Kwak, D.-U. Sim, J.H. Kwon, Y.J. Yoon, Design of PIFA with metamaterials for body-SAR reduction in wearable applications. *IEEE Trans. Electromagn. Compatib.* **59**(1), 297–300 (2016)
- 69 F. Hu, W. Wang, J. Cheng, Y. Bao, Origami spring-inspired metamaterials and robots: An attempt at fully programmable robotics. *Sci. Prog.* **103**(3), 0036850420946162 (2020)
- 70 A. Rafsanjani, K. Bertoldi, A.R. Studart, Programming soft robots with flexible mechanical metamaterials. *Sci. Robot.* **4**(29), 7874 (2019)
- 71 T.J. Sheng et al., An internet of things based smart waste management system using LoRa and tensorflow deep learning model. *IEEE Access* **8**, 148793–148811 (2020)
- 72 M. Shahidul Islam, M.T. Islam, A.F. Almutairi, G.K. Beng, N. Misran, Monitoring of the human body signal through the Internet of Things (IoT) based LoRa wireless network system. *Appl. Sci.* **9**(9), 1884 (2019)
- 73 P. Wang, M.E. Nasir, A.V. Krasavin, W. Dickson, Y. Jiang, A.V. Zayats, Plasmonic metamaterials for nanochemistry and sensing. *Acc. Chem. Res.* **52**(11), 3018–3028 (2019)
- 74 W. Li et al., Refractory plasmonics with titanium nitride: broadband metamaterial absorber. *Adv. Mater.* **26**(47), 7959–7965 (2014)
- 75 Y.-C. Lai, C.-Y. Chen, Y.-T. Hung, C.-Y. Chen, Extending absorption edge through the hybrid resonator-based absorber with wideband and near-perfect absorption in visible region. *Materials* **13**(6), 1470 (2020)
- 76 M.L. Hakim et al., Wide-oblique-incident-angle stable polarization-insensitive ultra-wideband metamaterial perfect absorber for visible optical wavelength applications. *Materials* **15**(6), 2201 (2022)
- 77 H. Luo, Y.Z. Cheng, Design of an ultrabroadband visible metamaterial absorber based on three-dimensional metallic nanostructures. *Mod. Phys. Lett. B* **31**(25), 1750231 (2017)
- 78 P. Yu et al., Ultra-wideband solar absorber based on refractory titanium metal. *Renewable Energy* **158**, 227–235 (2020)
- 79 N. Muhammad, T. Fu, Q. Liu, X. Tang, Z.-L. Deng, Z. Ouyang, Plasmonic metasurface absorber based on electro-optic substrate for energy harvesting. *Materials* **11**(11), 2315 (2018)
- 80 D. Katrodiya, C. Jani, V. Sorathiya, S.K. Patel, Metasurface based broadband solar absorber. *Opt. Mater.* **89**, 34–41 (2019)
- 81 J. Li et al., Broadband solar energy absorber based on monolayer molybdenum disulfide using tungsten elliptical arrays. *Mater. Today Energy* **16**, 100390 (2020)
- 82 Y. Lin et al., Tungsten based anisotropic metamaterial as an ultra-broadband absorber. *Optical Mater. Express* **7**(2), 606–617 (2017)
- 83 M. Chirumamilla et al., Thermal stability of tungsten based metamaterial emitter under medium vacuum and inert gas conditions. *Sci. Rep.* **10**(1), 3605 (2020)
- 84 N. Pirouzfam, K. Sendur, Tungsten based spectrally selective absorbers with anisotropic rough surface texture. *Nanomaterials* **11**(8), 2018 (2021)
- 85 M.M.K. Shuvo et al., Polarization and angular insensitive bendable metamaterial absorber for UV to NIR range. *Sci. Rep.* **12**(1), 4857 (2022)
- 86 M.M. Soliman et al., Broadband near unity absorption metastructure for solar thermophotovoltaic systems and optical window applications. *Nanoscale* **15**(31), 12972–12994 (2023)
- 87 E.J. Rothwell, J.L. Frasch, S.M. Ellison, P. Chahal, R.O. Ouedraogo, Analysis of the Nicolson-Ross-Weir method for characterizing the electromagnetic properties of engineered materials. *Prog. Electromag. Res.* **157**, 31–47 (2016)
- 88 J. Qu, H. Pan, Y.Z. Sun, H.F. Zhang, Multitasking Device Regulated by the Gravity Field: Broadband Anapole-Excited Absorber and Linear Polarization Converter. *Ann. Phys.* **534**(9), 2200175 (2022)
- 89 Y. Wen et al., A Multifunctional Integrated Design of Simultaneous Unity Absorption and Polarization Conversion. *Plasmonics* **15**, 1141–1149 (2020)
- 90 B. Liu et al., Broadband, wide-angle, and polarization-insensitive enhancement of light absorption in monolayer graphene over whole visible spectrum. *Results Phys.* **18**, 103134 (2020)
- 91 J. Kim, H. Oh, B. Kang, J. Hong, J.-J. Rha, M. Lee, Broadband visible and near-infrared absorbers implemented with planar nanolayered stacks. *ACS Appl. Nano Mater.* **3**(3), 2978–2986 (2020)
- 92 I. Hossain, M. Samsuzzaman, M. Moniruzzaman, B.B. Bais, M.S.J. Singh, M.T. Islam, Polarization-independent broadband optical regime metamaterial absorber for solar harvesting: A numerical approach. *Chin. J. Phys.* **71**, 699–715 (2021)
- 93 P. Pitchappa, C.P. Ho, P. Kropelnicki, N. Singh, D.-L. Kwong, C. Lee, Dual band complementary metamaterial absorber in near infrared region. *J. Appl. Phys.* (2014). <https://doi.org/10.1063/1.4878459>
- 94 U. Köse, E. Ekmekçi, The effects of the dielectric substrate thickness and the loss tangent on the absorption spectrum: a comprehensive study considering the resonance type, the ground plane coupling, and the characterization setup (2023)
- 95 Y. Zhou et al., Ultra-broadband metamaterial absorbers from long to very long infrared regime. *Light Sci. Appl.* **10**(1), 138 (2021)
- 96 G. Duan, J. Schalch, X. Zhao, J. Zhang, R. Averitt, X. Zhang, Identifying the perfect absorption of metamaterial absorbers. *Phys. Rev. B* **97**(3), 035128 (2018)

97. H. Wang, L. Wang, Perfect selective metamaterial solar absorbers. *Opt. Express* **21**(106), A1078–A1093 (2013)
98. X. Zeng, M. Gao, L. Zhang, G. Wan, B. Hu, Design of a triple-band metamaterial absorber using equivalent circuit model and interference theory. *Microw. Opt. Technol. Lett.* **60**(7), 1676–1681 (2018)
99. N.T.Q. Hoa, P.D. Tung, P.H. Lam, N.D. Dung, N.H. Quang, Numerical study of an ultrabroadband, wide-angle, polarization-insensitivity metamaterial absorber in the visible region. *J. Electron. Mater.* **47**, 2634–2639 (2018)
100. P. Zhu, L. Jay Guo, High performance broadband absorber in the visible band by engineered dispersion and geometry of a metal-dielectric-metal stack. *Appl. Phys. Lett.* **101**(24), 241116 (2012)
101. X. Zhang, Y. Fan, L. Qi, H. Li, Broadband plasmonic metamaterial absorber with fish-scale structure at visible frequencies. *Optic. Mater. Express* **6**(7), 2448–2457 (2016)
102. M.K. Hedayati et al., Design of a perfect black absorber at visible frequencies using plasmonic metamaterials. *Adv. Mater.* **23**(45), 5410–5414 (2011)
103. M. Luo, S. Shen, L. Zhou, S. Wu, Y. Zhou, L. Chen, Broadband, wide-angle, and polarization-independent metamaterial absorber for the visible regime. *Opt. Express* **25**(14), 16715–16724 (2017)
104. S. Butun, K. Aydin, Structurally tunable resonant absorption bands in ultrathin broadband plasmonic absorbers. *Opt. Express* **22**(16), 19457–19468 (2014)
105. A. Hoque, M.T. Islam, Numerical analysis of single negative broadband metamaterial absorber based on tri thin layer material in visible spectrum for solar cell energy harvesting. *Plasmonics* **15**(4), 1061–1069 (2020)

**Publisher's Note** Springer Nature remains neutral with regard to jurisdictional claims in published maps and institutional affiliations.

Springer Nature or its licensor (e.g. a society or other partner) holds exclusive rights to this article under a publishing agreement with the author(s) or other rightsholder(s); author self-archiving of the accepted manuscript version of this article is solely governed by the terms of such publishing agreement and applicable law.